

Analysis of the XENON100 Dark Matter Search Data

E. Aprile,¹ M. Alfonsi,² K. Arisaka,³ F. Arneodo,⁴ C. Balan,⁵ L. Baudis,⁶ A. Behrens,⁶ P. Beltrame,³ K. Bokeloh,⁷ E. Brown,⁷ G. Bruno,⁴ R. Budnik,¹ J. M. R. Cardoso,⁵ W.-T. Chen,⁸ B. Choi,¹ D. B. Cline,³ H. Contreras,¹ J. P. Cussonneau,⁸ M. P. Decowski,² E. Duchovni,⁹ S. Fattori,¹⁰ A. D. Ferella,⁶ W. Fulgione,¹¹ F. Gao,¹² M. Garbini,¹³ K.-L. Giboni,¹ L. W. Goetzke,¹ C. Grignon,¹⁰ E. Gross,⁹ W. Hampel,¹⁴ H. Kettling,⁷ A. Kish,⁶ J. Lamblin,⁸ H. Landsman,⁹ R. F. Lang,^{15,1} M. Le Calloch,⁸ C. Levy,⁷ K. E. Lim,¹ Q. Lin,¹² S. Lindemann,¹⁴ M. Lindner,¹⁴ J. A. M. Lopes,⁵ K. Lung,³ T. Marrodán Undagoitia,^{6,*} F. V. Massoli,¹³ Y. Mei,^{16,10} A. J. Melgarejo Fernandez,¹ Y. Meng,³ A. Molinario,¹¹ E. Nativ,⁹ K. Ni,¹² U. Oberlack,^{16,10} S. E. A. Orrigo,⁵ E. Pantic,^{3,†} D. Pätzold,¹⁰ R. Persiani,¹³ G. Plante,¹ N. Priel,⁹ A. Rizzo,¹ S. Rosendahl,⁷ J. M. F. dos Santos,⁵ G. Sartorelli,¹³ J. Schreiner,¹⁴ M. Schumann,⁶ L. Scotto Lavina,⁸ P. R. Scovell,³ M. Selvi,¹³ P. Shagin,¹⁶ H. Simgen,¹⁴ A. Teymourian,³ D. Thers,⁸ O. Vitells,⁹ H. Wang,³ M. Weber,¹⁴ and C. Weinheimer⁷

(The XENON100 Collaboration)

¹*Physics Department, Columbia University, New York, NY 10027, USA*

²*Nikhef and the University of Amsterdam, Science park, Amsterdam, Netherlands*

³*Physics & Astronomy Department, University of California, Los Angeles, USA*

⁴*INFN, Laboratori Nazionali del Gran Sasso, Assergi, 67100, Italy*

⁵*Department of Physics, University of Coimbra, R. Larga, 3004-516, Coimbra, Portugal*

⁶*Physics Institute, University of Zürich, Winterthurerstr. 190, CH-8057, Switzerland*

⁷*Institut für Kernphysik, Wilhelms-Universität Münster, 48149 Münster, Germany*

⁸*SUBATECH, Ecole des Mines de Nantes, CNRS/In2p3, Université de Nantes, 44307 Nantes, France*

⁹*Department of Particle Physics and Astrophysics, Weizmann Institute of Science, 76100 Rehovot, Israel*

¹⁰*Institut für Physik, Johannes Gutenberg Universität Mainz, 55099 Mainz, Germany*

¹¹*University of Torino and INFN-Torino, Torino, Italy*

¹²*Department of Physics, Shanghai Jiao Tong University, Shanghai, 200240, China*

¹³*University of Bologna and INFN-Bologna, Bologna, Italy*

¹⁴*Max-Planck-Institut für Kernphysik, Saupfercheckweg 1, 69117 Heidelberg, Germany*

¹⁵*Department of Physics, Purdue University, West Lafayette, IN 47907, USA*

¹⁶*Department of Physics and Astronomy, Rice University, Houston, TX 77005 - 1892, USA*

The XENON100 experiment, situated in the Laboratori Nazionali del Gran Sasso, aims at the direct detection of dark matter in the form of weakly interacting massive particles (WIMPs), based on their interactions with xenon nuclei in an ultra low background dual-phase time projection chamber. This paper describes the general methods developed for the analysis of the XENON100 data, focusing on the 100.9 live days science run from which results on spin-independent elastic and inelastic WIMP-nucleon cross-sections have already been reported.

Keywords: Dark Matter, WIMPs, Direct Detection, Xenon

I. INTRODUCTION

The XENON100 experiment aims to directly detect cold, non-baryonic dark matter which accounts for the majority of the matter in the Universe [1] according to plentiful astronomical and cosmological evidence. Among the most promising dark matter candidates are weakly interacting massive particles (WIMPs), arising naturally in several models beyond the Standard Model of particle physics [2]. If WIMPs are the dark matter particles, they could be directly detected via scattering off nuclei [3]. In this paper, the complete analysis of the low-energy XENON100 data is presented focusing on the 100.9 live days science run. The XENON100 collaboration previously reported exclusion limits on spin-

independent elastic [4] and inelastic [5] WIMP-nucleon scattering using this data set.

Following this introduction, Section II introduces the XENON100 experiment and details the formalism of the measurement process. Section III describes the data set, reconstruction procedures and selection cuts used in the analysis. This is followed by estimates of nuclear and electronic recoil backgrounds with control samples from Monte Carlo simulations, calibration data and science data outside of the signal region. Finally, a description of the observed event population and the comparison with the expected background is presented.

II. THE XENON100 EXPERIMENT

A. Instrument description

The XENON100 detector is filled with a total of 161 kg of ultra pure liquid xenon (LXe) divided in two concen-

*Electronic address: marrodan@physik.uzh.ch

†Electronic address: pantic@physics.ucla.edu

tric cylindrical volumes. The inner target volume is a two-phase (liquid/gas) time projection chamber (TPC) of 30.5 cm height and 15.3 cm radius containing a xenon mass of 62 kg. It is optically separated from the surrounding LXe veto, closed on the bottom by a cathode mesh and on the top by a gate and an anode mesh, which provide the homogeneous electric fields required for the operation of the TPC. A technique similar to the one of a diving bell was chosen to keep the liquid in the TPC at a precise level between the gate and the anode meshes and to raise the liquid level in the veto (outside of the bell) above the TPC. This enables full LXe coverage of the TPC for an efficient suppression of external radioactive backgrounds. The XENON100 instrument and its subcomponents are explained in detail in [6] and only a short summary is given here.

A particle interaction in the LXe target creates both excited and ionized atoms, which combine with the surrounding atoms to form excimers [7]. De-excitation of these excimers leads to a prompt xenon scintillation signal (S1), which is recorded by photomultiplier tubes (PMTs) placed below the target in the LXe and above in the gas phase. Due to the presence of an electric drift field of 530 V/cm, a large fraction of the ionization electrons is drifted away from the interaction site in the TPC with a drift velocity $v_d \simeq 1.73 \text{ mm}/\mu\text{s}$. Electrons which escape recombination and are not trapped by impurities are extracted from the liquid into the gas phase by a strong extraction field of $\sim 12 \text{ kV/cm}$, and a light signal (S2) is generated by proportional scintillation in the gas [8]. The S2 signal is detected by the same PMTs but is delayed by the drift time t_d , which is the time it takes the electrons to drift from the interaction site to the liquid/gas interface. 3-dimensional event vertex reconstruction is achieved using t_d and v_d to reconstruct the z position ($z = v_d t_d$) and the hit pattern on the PMTs in the gas phase to reconstruct the (x, y) position. The ratio S2/S1 is different for electronic recoil events from interactions with the atomic electrons (from γ and β backgrounds), and for interactions with the nucleus itself (nuclear recoils from WIMPs or neutrons), and is used to discriminate the signal against background.

The PMTs are 1 inch \times 1 inch Hamamatsu R8520, selected for high quantum efficiency (up to 32%) and very low intrinsic radioactivity. 80 tubes are immersed in the LXe below the TPC to ensure high light collection. 98 PMTs are placed in the gas phase above the target, arranged in concentric rings with the outmost ring extending beyond the TPC edge for improved (x, y) position reconstruction. The LXe layer surrounding the target is instrumented with 64 additional PMTs, observing the volumes above, below and on the sides of the TPC, and operating as an active LXe veto.

All materials used for the construction of the detector were selected for low intrinsic radioactivity [9], in order to minimize the electronic recoil background and neutron background from (α, n) and spontaneous fission reactions. To suppress the external background, the detec-

tor is installed inside a passive shield. From the inside to the outside this consists of 5 cm of oxygen free high conductivity copper, 20 cm of polyethylene, 5 cm of lead with a low ^{210}Pb concentration, and 15 cm of standard lead. Three sides and the top of the shield have 20-cm-thick water or polyethylene shielding to further lower the neutron background, and the entire shield installation sits on a 20 cm slab of polyethylene. The detector is installed underground in the Laboratori Nazionali del Gran Sasso (LNGS) in Italy, at an average depth of 3600 m water equivalent, which effectively reduces the muon flux by a factor of 10^6 compared to the surface flux [10].

B. Measurement process and event rates

This section describes the formalism of light and charge detection in XENON100. Upper case latin letters in S1 and S2 are used for the actual measured quantities while lower case letters in s1 and s2 denote expectation values. P is a discrete probability and p is a probability density function (pdf).

1. Generation of light and charge

For a given energy deposit of an interaction type u ($u \equiv \text{nr}$ for nuclear recoil and $u \equiv \text{ee}$ for electronic recoil) E_u in the presence of a drift field of strength \mathcal{E} , the combined probability $P(N_\gamma, N_e | E_u, \mathcal{E})$ for the generation of N_γ photons and N_e electrons shows, in general, an anti-correlation between the number of free electrons and photons. This is due to charge recombination processes which can lead to additional scintillation light [7]. At low energy deposits, such as for nuclear recoils in the dark matter region of interest, however, the measurement uncertainties dominate the width of the observed probability distributions [11]. Hence, P can be approximated by independent Poisson processes:

$$P(N_\gamma, N_e | E_u, \mathcal{E}) \approx \text{Poi}(N_\gamma | n_\gamma) \text{Poi}(N_e | n_e). \quad (1)$$

The average energies needed for creation of one information carrier (photon or free electron) are expressed by effective “ W -values”, which depend on the interaction type, the drift field, and, at low energies, also on the deposited energy. The field dependence can be factorized with functions S_u for the reduction in light yield due to field quenching and T_u for the loss of charge due to recombination. The expectation values $n_\gamma(E_u, \mathcal{E})$ and $n_e(E_u, \mathcal{E})$ can then be written as

$$\begin{aligned} n_\gamma(E_u, \mathcal{E}) &= \frac{E_u}{W_\gamma(E_u, \mathcal{E})} \approx \frac{E_u}{W_\gamma(E_u, \mathcal{E} = 0)} S_u(\mathcal{E}), \quad (2) \\ n_e(E_u, \mathcal{E}) &= \frac{E_u}{W_e(E_u, \mathcal{E})} \approx \frac{E_u}{W_e(E_u, \mathcal{E}_{\text{ref}} \rightarrow \infty)} T_u(\mathcal{E}), \quad (3) \end{aligned}$$

where $S_u(0) = 1$ and $T_u(\mathcal{E}_{\text{ref}} \rightarrow \infty) = 1$.

In xenon dark matter detectors, the energy calibration of nuclear recoils is accomplished by comparing the signals from known γ -ray lines to dedicated measurements of the functions W_γ and S_u , or W_e and T_u , which differ for electronic and nuclear recoils. In order to minimize the systematic uncertainties of the cross-calibration resulting from modeling the detector responses, a reference source is frequently used. Historically, this has been the 122 keV_{ee} line from ^{57}Co decay, where the keV_{ee} represents the electronic-equivalent recoil energy. The in situ measured light and charge yields at 122 keV_{ee} can be used as fixed points to establish the energy scale at lower γ -ray energies and for nuclear recoils, using the ratios of $W_\gamma(E_u)$ and $W_e(E_u)$ relative to this reference, and applying the functions $S_u(\mathcal{E})$ and $T_u(\mathcal{E})$, respectively. Currently, for nuclear recoils ($E_u \equiv E_{\text{nr}}$), $W_\gamma(E_{\text{nr}})$ [12] has been measured to lower energies than $W_e(E_{\text{nr}})$. Hence, XENON100 uses the primary scintillation light to establish the energy scale.

2. Measurement of primary scintillation light

The expectation value for the primary scintillation light signal S1 on PMT i with a gain g_i , after integrating the current pulse is given in units of electron charge

$$s1_i^q(\vec{r}) = n_\gamma(E_u, \mathcal{E}) \gamma_i(\vec{r}) \eta_i g_i = n_\gamma(E_u, \mathcal{E}) \mu_i(\vec{r}) g_i, \quad (4)$$

where $\gamma_i(\vec{r})$ is the probability for a photon created at position \vec{r} within the TPC to reach the photocathode of PMT i and η_i is the product of quantum and collection efficiencies for that PMT. The combined function $\mu_i(\vec{r})$ is the light detection efficiency and is measured with γ -ray calibrations (see Sec. III C). The raw data processor converts the measured signal into units of photoelectrons, using the estimates of gains which include an amplification factor of 10 [6]. Since errors in the determination of the combined PMT and amplification gains are typically $< 2\%$ [6], these will be neglected in the following. Hence the expectation value for the primary scintillation signal on PMT i in units of photoelectrons (PE) is

$$s1_i(\vec{r}) \approx n_\gamma(E_u, \mathcal{E}) \mu_i(\vec{r}). \quad (5)$$

If M is the number of PMTs in the TPC, the energy deposit for nuclear recoils E_{nr} determines the expected total primary scintillation signal s1 as

$$\begin{aligned} s1(\vec{r}) &= \sum_{i=1}^M s1_i(\vec{r}) \approx n_\gamma(E_{\text{nr}}, \mathcal{E}) \mu(\vec{r}) \\ &= E_{\text{nr}} \mathcal{L}_y(E_{\text{ee}} = E_{\text{ref}}, \mathcal{E}, \vec{r}) \\ &\quad \times \mathcal{L}_{\text{eff}}(E_{\text{nr}}, \mathcal{E} = 0) \frac{S_{\text{nr}}(\mathcal{E})}{S_{\text{ee}}(\mathcal{E})}, \end{aligned} \quad (6)$$

where $\mu(\vec{r}) = \sum_i \mu_i(\vec{r})$. \mathcal{L}_y is the measured light yield for a reference γ -ray line (in PE/keV_{ee}) at the given electric field and position [see Eqs. (2) and (5)], given as

$$\mathcal{L}_y(E_{\text{ee}} = E_{\text{ref}}, \mathcal{E}, \vec{r}) = \frac{S_{\text{ee}}(\mathcal{E}) \mu(\vec{r})}{W_\gamma(E_{\text{ee}} = E_{\text{ref}}, \mathcal{E} = 0)}. \quad (7)$$

\mathcal{L}_{eff} is the relative scintillation yield of nuclear recoils with respect to the reference γ -ray line at zero field, which equals

$$\mathcal{L}_{\text{eff}}(E_{\text{nr}}, \mathcal{E} = 0) = \frac{W_\gamma(E_{\text{ee}} = E_{\text{ref}}, \mathcal{E} = 0)}{W_\gamma(E_{\text{nr}}, \mathcal{E} = 0)}. \quad (8)$$

S_{nr} and S_{ee} are the reductions in light yield due to field quenching for nuclear and electronic recoils, respectively. Solving Eq. (6) for a measured signal S1 results in the nuclear-equivalent recoil energy estimate E_{nr} , which is position-dependent. However, the data analysis is usually performed with the “spatially-corrected” measured signal

$$\text{cS1} \equiv \text{S1}(\vec{r}) \frac{\langle \mu \rangle}{\mu(\vec{r})}, \quad (9)$$

where μ is the estimate for the sum over all PMTs and $\langle \mu \rangle$ is the spatial average. For such spatially-corrected signal, cS1 corresponds to the detector-averaged signal expectation value

$$\text{cS1} \approx E_{\text{nr}} \langle \mathcal{L}_y(E_{\text{ref}}, \mathcal{E}) \rangle \mathcal{L}_{\text{eff}}(E_{\text{nr}}, \mathcal{E} = 0) \frac{S_{\text{nr}}(\mathcal{E})}{S_{\text{ee}}(\mathcal{E})}, \quad (10)$$

where $\langle \mathcal{L}_y \rangle$ is the detector-averaged light yield. From Eqs. (9) and (10) for a measured cS1, using the in situ measured light yield estimate $\langle \mathcal{L}_y \rangle$ and $\mathcal{L}_{\text{eff}}(E_{\text{nr}})$, S_{nr} and S_{ee} from either dedicated measurements or in-situ evaluations, one can obtain the detector-averaged nuclear recoil energy estimate $\langle E_{\text{nr}} \rangle$.

Assuming a Poisson-distributed number of generated photons N_γ and a binomially distributed number of generated photoelectrons for each PMT $N_{pe,i}$, the pdf is described by

$$\begin{aligned} p_{\text{S1},i}(\text{S1}_i | n_\gamma(E_u, \mathcal{E})) d\text{S1}_i &= \sum_{N_{pe,i}} \sum_{N_\gamma} p_{\text{pmt},i}(\text{S1}_i | N_{pe,i}) d\text{S1}_i \\ &\quad \times \text{Binom}(N_{pe,i} | N_\gamma, \mu_i(\vec{r})) \\ &\quad \times \text{Poi}(N_\gamma | n_\gamma(E_u, \mathcal{E})) \\ &= \sum_{N_{pe,i}} p_{\text{pmt},i}(\text{S1}_i | N_{pe,i}) \\ &\quad \times \text{Poi}(N_{pe,i} | n_\gamma, \mu_i(\vec{r})) d\text{S1}_i, \end{aligned} \quad (11)$$

where $p_{\text{pmt},i}(\dots)$ is the response of PMT i , approximated by a Gaussian with mean value $N_{pe,i}$ and width

$\sigma_i/\sqrt{N_{pe,i}}$. The detected photoelectron width σ_i is determined from PMT calibrations.

Taking into account that $S1 = \sum_{i=1}^M S1_i$ the pdf for the total light signal S1 can be calculated from Eq. (11) as

$$p_{S1}(S1|n_\gamma(E_u, \mathcal{E})) dS1 = \left(\int \cdots \int_{1 \dots M} \prod_{i=1}^M p_{S1,i}(S1_i | n_\gamma) \times \delta(S1 - \sum_{j=1}^M S1_j) dS1_1 \dots dS1_M \right) dS1. \quad (12)$$

This formula can be evaluated by computer simulations using individual response tables for each PMT.

3. Measurement of charge

The ionization electrons produced at an interaction point drift through the liquid, where losses due to attachment to electronegative impurities with characteristic time τ_e occur (see Sec. III C). Electrons reaching the liquid surface are extracted into the gas phase with a yield κ that depends on the extraction field \mathcal{E}_{gas} . The same field is responsible for the proportional scintillation light signal S2 [8] resulting in an amplification factor Y from scattering of accelerated electrons with gas atoms. The expectation value for the secondary scintillation light signal on PMT i in units of PE is described by

$$s2_i(\vec{r}) \approx n_e(E_u, \mathcal{E}) e^{-t_d/\tau_e} \kappa(\mathcal{E}_{\text{gas}}) Y \left(\frac{\mathcal{E}_{\text{gas}}}{\rho}, h_g \right) \beta_i(x, y) \eta_i. \quad (13)$$

Y is also called secondary scintillation gain and it depends on the ratio of \mathcal{E}_{gas} to the gas density ρ , and on the size of the gas gap h_g . Due to mesh warping or to an inclined liquid level, \mathcal{E}_{gas} and h_g can be (x, y) position dependent. $\beta_i(x, y)$ is the probability for a photon created at the position (x, y) in the gas gap to reach the photocathode of the PMT i . Since the S2 signal is created in a narrow gas gap ($h_g \sim 2.5$ mm), $\beta_i(x, y)$ can be considered as a function of (x, y) only. Gamma calibration lines can be used to measure the product $\delta_i = \kappa Y \beta_i \eta_i$. Currently, only the sum over the PMTs is measured, resulting in an estimate $\delta(x, y) = \sum_i \delta_i(x, y)$. The analysis is usually performed with the corrected measured signal:

$$cS2 \equiv S2(\vec{r}) e^{t_d/\tau_e} \frac{\langle \delta \rangle}{\delta(x, y)}. \quad (14)$$

Using Eqs. (3) and (13), the expected total secondary scintillation signal for nuclear recoils can be written as

$$s2(\vec{r}) = \sum_i s2_i(\vec{r}) = E_{\text{nr}} Q_y(E_{\text{nr}}) e^{-t_d/\tau_e} \delta(x, y), \quad (15)$$

where $Q_y = T_{\text{nr}}(\mathcal{E})/W_e(E_{\text{nr}}, \mathcal{E}_{\text{ref}})$ is the measured charge yield of nuclear recoils (in $e^-/\text{keV}_{\text{nr}}$) at the given electric field. The pdf $p_{S2,i}(S2_i)$ can be described as

$$p_{S2,i}(S2_i | n_e(E_u, \mathcal{E})) dS2_i = \sum_{N_{pe,i}} p_{\text{pmt},i}(S2_i | N_{pe,i}) \times \text{Poi}(N_{pe,i} | n_e, \delta_i) dS2_i, \quad (16)$$

where $p_{\text{pmt},i}$ is the same response of PMT i as in Eq. (11). The pdf for the total proportional scintillation light signal S2, denoted by $p_{S2}(S2 | n_e(E_u, \mathcal{E}))$, can be evaluated analogously to Eq. (12).

4. Event rate calculation

The measured differential nuclear recoil rate $d^2 R/dS1 dS2$ for a given WIMP-nucleus scattering rate dR/dE_{nr} is computed as

$$\begin{aligned} \frac{d^2 R}{dS1 dS2} &= \epsilon(S1, S2) \int \frac{dR}{dE_{\text{nr}}} p(S1, S2 | E_{\text{nr}}) dE_{\text{nr}} \\ &\approx \epsilon_{1,s}(S1) \epsilon_{2,s}(S2) \int \frac{dR}{dE_{\text{nr}}} \\ &\quad \times p_{S1}(S1 | E_{\text{nr}}) p_{S2}(S2 | E_{\text{nr}}) dE_{\text{nr}}, \end{aligned} \quad (17)$$

where $\epsilon_{1,s}(S1)$ and $\epsilon_{2,s}(S2)$ are the S1 and S2 signal detection efficiencies for the applied selection criteria on the data. These are a combination of the trigger threshold, event search algorithm and event selection cuts, where cuts can be applied on both spatially corrected and uncorrected S1 and S2 signals.

As already mentioned, so far the relation between E_{nr} and S1 signal has been measured more precisely and down to lower energies ($n_\gamma(E_{\text{nr}}, \mathcal{E})$ via $\mathcal{L}_{\text{eff}}(E_{\text{nr}})$) than the relation between E_{nr} and S2 signal ($n_e(E_{\text{nr}}, \mathcal{E})$ via $Q_y(E_{\text{nr}})$; see Fig. 5 of reference [13]). Therefore, the analysis is done using only the measured differential rate expressed in the cS1 signal as

$$\begin{aligned} \frac{dR}{dcS1} &= \int \frac{dR}{dE_{\text{nr}}} \epsilon_1(cS1) \int p_{S1}(S1(\vec{r}) | E_{\text{nr}}) \frac{\mu(\vec{r})}{\langle \mu \rangle} d\vec{r} \\ &\quad \times \underbrace{\int_{S2_{\text{min}}} p_{S2}(S2 | E_{\text{nr}}) \epsilon_{2,s}(S2) dS2}_{\epsilon_{2,E}(E_{\text{nr}} \propto cS1)} dE_{\text{nr}}, \end{aligned} \quad (18)$$

where for most of the selection criteria the efficiency is estimated in the spatially-corrected S1 signal $\epsilon_1(cS1)$. The exception is the S2 threshold cut ($S2_{\text{min}}$), which directly

influences the corresponding S1 signal efficiency via energy sharing at the level of generated n_γ and n_e before the Poisson fluctuations and the measurement uncertainties. Hence its acceptance $\epsilon_{2,E}$ is calculated as a function of the detector-averaged expectation value cs1 (see Sec. III E 2), which is related to nuclear recoil energy E_{nr} via Eq. (10). For notation simplicity, in the rest of the paper we use S1 and S2 instead of the corrected quantities cs1 and cs2 , unless explicitly specified.

III. DATA ANALYSIS

This section presents the complete analysis associated with the 100.9 live days dark matter search run acquired in 2010. The data set, analysis methods, event selection and acceptances, and the background predictions are described in detail. This analysis has been used to obtain a result which has been already interpreted in terms of spin-independent elastic [4] and inelastic [5] WIMP-nucleon interactions.

A. Data set

The data used in this analysis were selected from periods with stable detector operating conditions. Periods with xenon pressure and temperature values being more than 5 sigma away from the average value were excluded from the analysis. After this selection, other parameters like LXe level, cryostat vacuum pressure, purification flow and pulse tube refrigerator temperature were found to be stable during the whole science run. Figure 1 shows the time evolution of the xenon pressure and temperature over the entire length of the run, including correlated fluctuations. A 5 sigma variation corresponds to ± 0.04 K (0.04%) and ± 0.005 atm (0.24%) in temperature and pressure, respectively.

The high voltages biasing the cathode at -16 kV and anode at $+4.5$ kV were continuously monitored. The cathode was stable over the complete period while the anode had 9 trips due to the anode current exceeding a predefined threshold. Data from 20 minutes before the trip until 20 minutes after restoration of 4.5 kV were removed from the analysis, and the livetime was corrected accordingly. About 2% of the data was removed due to variations in the detector's operation parameters.

The radon concentration in the XENON room and inside the shield cavity were measured using dedicated radon monitors¹. The radon concentration in the XENON room was about 350 Bq/m^3 (see Fig. 7 in [14]) and found to be stable for the whole period. The volume inside the shield cavity was constantly flushed with boil-off nitrogen gas, resulting in a radon concentration

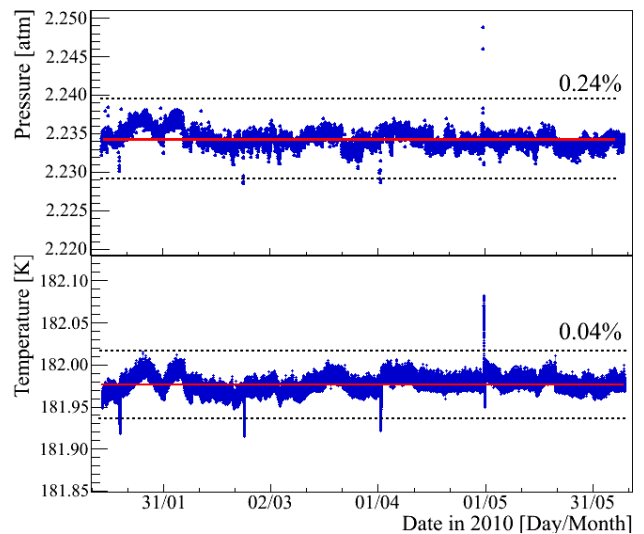


FIG. 1: Pressure and temperature of the XENON100 detector during the science run. The dotted lines represent the maximum allowed variations and data periods falling outside are removed from the run selection.

$< 1 \text{ Bq/m}^3$ throughout the run, at the radon monitor detection limit and consistent with zero. The measured electronic recoil background rate was found to be stable over the whole time in various energy intervals. A period of 18 live days was removed from the data due to an increased level of electronic pick-up noise.

The PMT gains were monitored with weekly LED calibrations and found to be stable within 2% which is given by the precision of the measurement. Weekly ^{137}Cs calibration data (γ -ray line at $662 \text{ keV}_{\text{ee}}$) were used to study the evolution of the light yield, charge yield, LXe purity, as well as the width of S2 pulses. The data was stable during the whole run and the LXe purity was continuously increasing (see Fig. 3).

The science run started on January 13th, 2010 and ended June 8th, 2010. Taking into account time periods removed due to the above-mentioned instabilities, anode trips, high electronic noise levels and DAQ dead time (about 10% in this run), the total live time used for this analysis is 100.9 live days.

B. Data acquisition and calibration

For low-energy signals, the detector was triggered on S2 pulses using the analog sum of 68 PMTs in the inner part of the top array and 16 PMTs in the center of the bottom array. In order to trigger on very small S2 pulses with typical $1 \mu\text{s}$ spread, the trigger signal was amplified, integrated and shaped with a spectroscopy amplifier, passed through a low threshold discriminator, and distributed simultaneously to the ADCs. The trigger threshold was measured directly using a dedicated background data. For this measurement, the discrim-

¹ RAD7 from DurrIDGE.

inated trigger signal was split using a Fan-In/Fan-Out module, with one output distributed to the ADCs to trigger and the other one fed into an ADC channel to be recorded. The major S2 peak, which triggers the data acquisition, is usually followed by small S2 peaks (see Fig. 17). These mainly consist of single to few electrons events emitted in the gas phase due to photoionization of impurities in liquid xenon by the prompt or proportional scintillation photons [15]. Any additional trigger raised by the discriminator for any of the secondary S2 peaks was recorded in the trigger channel. The ratio between the S2 spectrum generating the signal in the trigger channel and the full S2 input spectrum gives the trigger function. Figure 2 shows the result of the trigger roll-off measurement.

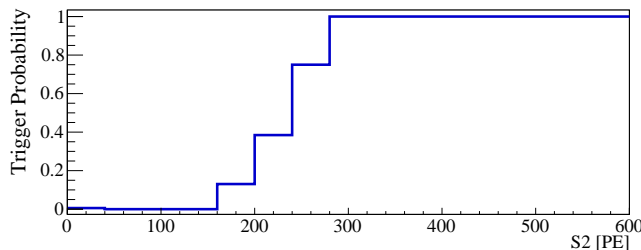


FIG. 2: Trigger probability as a function of the S2 signal size.

The background distribution due to electronic recoils is determined using the flat low-energy Compton continuum spectrum (see Sec. III F). A total of 5.8 live days of ^{60}Co calibration data were acquired, spread in time over the run. The source was placed at three different positions around the detector to evenly cover the sensitive LXe volume of the TPC.

The nuclear recoil (signal) region is defined using elastic neutron interactions from 2.9 live days of $^{241}\text{AmBe}$ data, acquired right before the dark matter run. Most of the data quality cuts and their acceptance have been defined on these data (see Sec. III E).

The irradiation of LXe with neutrons also gives γ -ray lines at $40\text{ keV}_{\text{ee}}$ and $80\text{ keV}_{\text{ee}}$ from ^{129}Xe and ^{131}Xe , respectively. The xenon isotopes are also activated leading to delayed de-excitation lines mainly at $164\text{ keV}_{\text{ee}}$ ($\tau_{1/2} = 11.8\text{ d}$) and $236\text{ keV}_{\text{ee}}$ ($\tau_{1/2} = 8.9\text{ d}$) from $^{131\text{m}}\text{Xe}$ and $^{129\text{m}}\text{Xe}$, respectively. Some of these lines are used to define position corrections for the S1 and S2 signals.

The energy scale for nuclear recoils (E_{nr}) is inferred from the cS1 signal via Eqs. (9) and (10). The scintillation efficiency $\mathcal{L}_{\text{eff}}(E_{\text{nr}})$ of nuclear recoils relative to $122\text{ keV}_{\text{ee}}$ is parametrized using all existing direct measurements as shown in [4]. The scintillation quenching factors due to the applied electric field for electronic recoils $S_{\text{ee}} = 0.58$ and nuclear recoils $S_{\text{nr}} = 0.95$ are taken from [16]. The light yield at $122\text{ keV}_{\text{ee}}$ is $\langle \mathcal{L}_y \rangle = (2.20 \pm 0.09)\text{ PE/keV}_{\text{ee}}$ and is interpolated using the light yields from the $40\text{ keV}_{\text{ee}}$, $80\text{ keV}_{\text{ee}}$, $164\text{ keV}_{\text{ee}}$ and $662\text{ keV}_{\text{ee}}$ lines [6].

The science data in the nuclear recoil region was

blinded and therefore not accessible until the analysis was finalized. The lower 90% quantile of the S2/S1 discrimination parameter for ^{60}Co electronic recoils determined the blinding cut for energies $S1 < 160\text{ PE}$. The data outside of the blinded region was also used for the estimation of the electronic recoil background in the WIMP signal region (see Sec. III F), for monitoring of the rate stability as well as for the estimation of the acceptances of certain data quality cuts.

C. Data processing

The digitized waveform from each of the 242 PMTs used in XENON100 are recorded. The trigger is located in the middle of the waveform, $400\text{ }\mu\text{s}$ long, and its global time is saved for each event. The raw data processor is based on the ROOT analysis toolkit [17]. It utilizes the difference in the S1 and S2 peak width, where the former is of the order of a few tens of ns (see Fig. 6) mainly governed by the LXe scintillation decay time constants [18] and the latter is of the order of a few μs determined by the electron cloud diffusion during the drift in the liquid and the drift time across the gas gap (see Fig. 9). For each peak candidate found by the processor, several peak properties are calculated and stored, for example pulse area (in PE), height (in V), width (in ADC samples with 1 sample = 10 ns), etc. More details can be found in [6][19].

For each identified S2, the (x, y) position is calculated using the hit pattern of the S2 photons in the top PMT array. Three independent algorithms were developed to reconstruct the position of each event. While an algorithm based on a neural network (NN) [20] is used for the analysis, the results from the two other algorithms (based on χ^2 minimization and using support vector machines, SVM [21]) are used for quality cross checks, see [6]. 3 mm and 0.3 mm position resolutions (1σ) in (x, y) and in z are obtained, respectively. Because of the finite S2 signal width, only pulses which are more than 3 mm apart in z can be separated.

An energy deposit will produce a different number of detected S1 photons depending on its position in the TPC. Primarily, this is due to the different paths that the light travels until a PMT is hit. A 2D axial-symmetric S1 light collection map $\mu(r, z)$, determined from monoenergetic lines, is applied to each measured S1 light pulse to obtain the position-corrected value [see Eq. (9)]. The maps derived using the $40\text{ keV}_{\text{ee}}$, $164\text{ keV}_{\text{ee}}$ and $662\text{ keV}_{\text{ee}}$ lines agree within 3%.

Similarly, there are position-dependent effects in the detection of the S2 signal [see Eq. (14)]. A (x, y) light collection map $\delta(x, y)$ is calculated, also from monoenergetic lines, using only the sum of S2 signals in the bottom PMT array ($S2_b$) as it has a more homogeneous light collection efficiency. The maximum (x, y) correction in the 48 kg fiducial mass, selected for the analysis (see III E 5), was 15%. An additional correction in z is necessary due

to absorption of ionization electrons by electronegative impurities in LXe during their drift. The electron lifetime τ_e , which is the time at which the total number of electrons produced is reduced by $1/e$ [see Eq. (13)], is used to quantify this effect [6]. The purity of the LXe was constantly increasing as monitored using the ^{137}Cs full absorption peak due to the continuous purification of the xenon gas by a hot getter. Figure 3 shows the time evolution of τ_e , which increased from $230\text{ }\mu\text{s}$ to $380\text{ }\mu\text{s}$ during this science run corresponding to a mean free path of 40 cm to 66 cm. A linear fit is used to describe the data and the time-dependent S2 drift time correction was applied accordingly. Since the maximum drift distance is

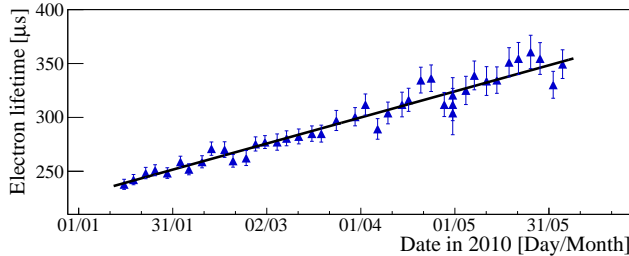


FIG. 3: Time evolution of the electron lifetime during the science run. A linear fit is used to describe the data.

30 cm, the maximal drift time correction was smaller than a factor of 2.

D. Analysis methods

Two parallel analyses were performed to interpret these data in a spin-independent WIMP-nucleon interaction framework as published in [4]. The energy region used for both analyses was $(4 - 30)$ PE in S1 (see III E 2) corresponding to $(8.4 - 44.6)$ keV_{nr}. Before unblinding, it was decided to use the Profile Likelihood analysis method [22] as the primary interpretation method which does not employ a fixed discrimination in S2/S1 parameter space. The calibration data sets were divided into 12 bands along $\log_{10}(\text{S2}_b/\text{S1})$, in a way that for every S1 bin the signal-like events are equally distributed between the bands (see Fig. 12). The number of bands was optimized based on the binning resolution of the discrimination parameter $\log_{10}(\text{S2}_b/\text{S1})$ and the available amount of calibration data in each band. The total number of events from calibration data in the preselected energy region was about 4300 for electronic recoils and about 76800 for nuclear recoils. While a large number of bands yields a result which depends less on the location of the event with respect to the band boundaries, the statistical uncertainty on the signal fraction in each band increases. It was verified that the results are robust to the number of bands, see also [22]. The background region consisting of Gaussian and anomalous contributions (see Sec. III F) is characterized using ^{60}Co calibration and non-blinded science data. The spectral shape of the neutron back-

ground is taken from Monte Carlo simulations [23]. Each signal or background event has an associated probability to fall into a certain band. Based on the event distribution for signal and background on these bands, both the signal-plus-background and the background-only hypotheses were tested regardless of the observed data. In the case of the exclusion of the signal hypothesis, the resulting limit on the WIMP-nucleon cross section is given at 90% confidence level (CL).

A cut-based analysis was also performed in [4] to cross check the result. This analysis uses the optimum interval method [24] to derive a 90% CL limit on the WIMP-nucleon cross section. The observed number of events in the pre-defined $\log_{10}(\text{S2}_b/\text{S1})$ signal region (benchmark WIMP search region) can be directly compared with the background prediction. For this analysis, after all selection criteria applied, the benchmark region was constrained by the 99.75% electronic recoil rejection line defined using ^{60}Co data, the 3σ lower contour of the nuclear recoil distribution, the S1 energy range and the threshold condition $\text{S2} > 300$ PE (see Sec. III E 5).

E. Dark matter search event selection

This section describes the criteria applied to the science data to select candidate events in the energy region of interest, which fall into the following general categories: data quality cuts, energy selection and threshold cut on S2, selection of single scatter events, consistency cuts, selection of the fiducial volume, and the signal region selection for the cut-based analysis.

The acceptance loss for each condition is determined using the fraction of events removed by this selection alone. For the case of independent selection cuts, this method gives a better estimate of the acceptance than using the fraction of the total events which pass the cut under study. The reason is that events which fail multiple cuts are far less likely to be valid events. For the cases in which the selection cuts were found not to be independent, their combined acceptance is derived. Visual inspection of a subset of both accepted and rejected event waveforms was used as a cross-check to validate the acceptance determination. The acceptance was evaluated using the energy range and the 48 kg fiducial mass, selected for the analysis (see III E 2 and III E 5). Nuclear recoil data is used to determine the acceptance for most of the cuts, with the few exceptions where conditions of neutron calibration datasets were found not to be representative for the full science data taking conditions.

1. Data quality

Data quality cuts remove non-physical or noisy waveforms. A two-fold PMT time-coincidence within a 20 ns time window is required for a valid S1, where each PMT hit must have a signal size larger than 0.35 PE. This effi-

ciently rejects PMT dark current signals as they are unlikely to happen simultaneously in multiple PMTs. Additionally, the S1 coincidence requirement was tightened for the pulses where the S1 peak contains noisy PMT channels. If known noisy PMTs contribute to the S1 coincidence, then the coincidence requirement is increased by the number of noisy PMTs [4] to avoid identification of an S1 candidate with only one good PMT.

For the results presented in [4, 5], the acceptance was computed via a Monte Carlo simulation, which takes into account light collection in the TPC, PMT quantum efficiencies, single photoelectron resolution, and the time dependence of the scintillation process. Using this method, the acceptance was estimated to be $>99\%$ above 6 PE and dropping down to 97% at 4 PE. However, the acceptance of this cut can be evaluated using data instead of a Monte Carlo simulation. Events from nuclear recoil calibration data with a coincident signal in the veto are used to compute the acceptance of the coincidence requirement, as they correspond to true physical interactions in the TPC. The acceptance is $>99\%$ above 10 PE and drops down to 80% at 4 PE (see Fig. 4). This new method gives a slightly lower acceptance compared to the previous one, but this has a negligible impact on the interpretation of the results in [4, 5]. Since the data-driven method gives a better estimate of the cut acceptance it is used in the upcoming data analysis.

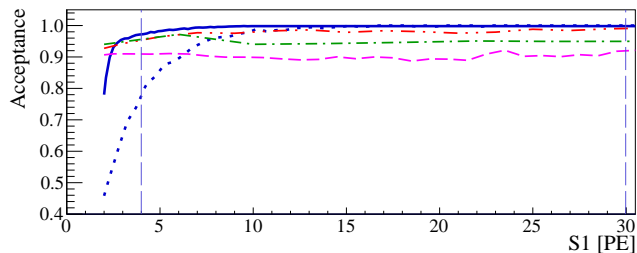


FIG. 4: Acceptance of some of the cuts as a function of S1: S1 coincidence requirement using the published Monte-Carlo-derived (solid blue) and new data-driven (dotted blue) methods, waveform quality cut using S1 and S2 candidate peak area (red dash-dot-dotted), S2 single scattering (green dash-dotted), and S2 pulse width cut (magenta dashed). The vertical lines represent the energy window for the analysis, see Sect. III E 2.

A population of events with an S1 peak due to noise was found after unblinding in the region around and below the analysis threshold of 4 PE. This population is due to electronic pick-up noise and not related to physical events in the TPC. Since the original cuts were not sufficiently restrictive against electronic noise, two additional cuts had to be introduced post-unblinding in order to remove the full noise population, including three noise events with S1 signal leaking above 4 PE. The S1 coincidence requirement was modified by adding few more noisy and non-functional PMT channels. The latter are turned off but can still pick-up electronic noise. An example of a rejected noise event is shown in Fig. 5. The

modification of the S1 coincidence requirement had no relevant impact on the nuclear recoil acceptance ($< 0.4\%$ acceptance loss) as determined on $^{241}\text{AmBe}$ calibration data.

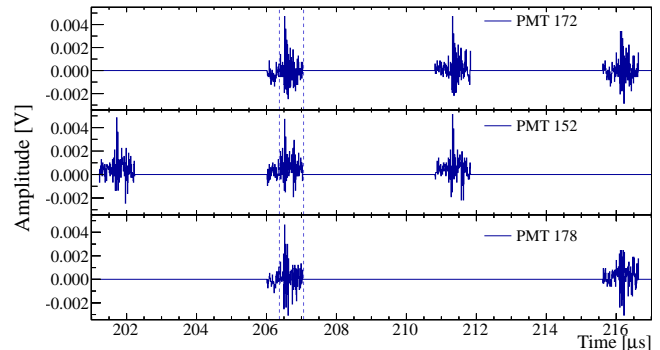


FIG. 5: PMT traces for a noise event found after unblinding. The S1 candidate region is indicated by blue dashed lines. All PMT signals contributing to the S1 candidate are periodic electronic pick-up noise peaks. The bottom panel shows a non functional PMT.

In addition, a cut on the S1 width was introduced. Figure 6 shows the histogram of the S1 peak width, defined between the right and left peak boundaries at 10% of the height. The distribution has a regular structure

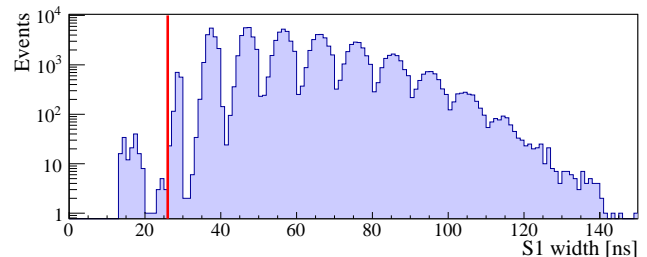


FIG. 6: Histogram of the S1 width at 10% level for neutron data. The line represents the cut on this parameter, events left of the line are rejected to eliminate electronic noise.

due to the finite sampling frequency of 100 MHz. Very small widths correspond to electronic noise pulses with samples fluctuating around the baseline, shortening the extent of the identified peak due to negative excursions (see Fig. 5). Events left of the vertical line are rejected. The line was defined after visual inspection of waveforms from $^{241}\text{AmBe}$ and low energy science data. Waveforms of valid events passing all cuts are shown in Fig. 17. The S1 width cut has an acceptance of 99.9% at 4 PE increasing to $>99.9\%$ above 6 PE, as verified with nuclear recoils.

The peak finding algorithm is tuned to correctly identify low-energy interactions with the highest possible acceptance. In waveforms of events with large energy depositions in the TPC (e.g. through-going muons) or with HV-induced micro-discharges, features in the pulse shape can sometimes be mistaken by the algorithm as individ-

ual small energy signals. The event selection requires that the integral of the largest S1 and S2 signals is bigger than the size of the integral of the remaining waveform. In order to obtain a sample with DAQ conditions representative of the full science run, the acceptance of this cut was calculated using science data outside of the blinded region. The cut acceptance in the energy region of interest is about 98% (see Fig. 4).

There are events where no valid S1 peak is present in the waveform. Such events appear either if the real S1 is too small to be detected or is missed by the peak-finder, or if it is too close to the S2 peak to be resolved as an individual peak. The latter mostly happens for interactions at the very top layer of LXe or in the gas region. In these events, a random electronic noise or a coincident PMT dark current peak can be picked up as an S1 candidate. Their very asymmetric S2 signal distribution on the top and the bottom PMT arrays can be used to identify and reject them. This selection was defined using the non-blinded part of the science data. The cut acceptance was determined to be $\sim 99.6\%$ in the energy range of $(4 - 30)$ PE using neutron calibration data.

Occasionally, S2-like events with signals very localized in the (x, y) plane and/or unusual light patterns occur. Two classes of such spurious events were found in some of the science data outside of the blinded region. In the first class, the events have the bulk of S2 light detected by a single PMT. As the maximal fraction of the S2 light seen by a single PMT has a mean value of about 20%, events are rejected when this fraction is more than 65%. In the second class, events have an unusually small fraction of S2 light detected by the top PMT array. Since the S2 signal is generated in the gas phase, the top PMT array typically sees about 1.3 times more proportional scintillation light than the bottom array. Hence events are removed when the amount of S2 light detected by the top array is less than 74% of the light in the bottom array. Both cuts were optimized using the non-blinded science data. Their acceptance was calculated using nuclear recoil data and it is above 99.6%.

2. Energy selection and S2 signal threshold

As already mentioned, the S1 energy region used for the analysis ranges from 4 to 30 PE. The selection acceptances above 4 PE were found to be high and nearly energy independent, while no notable WIMP sensitivity was gained by increasing the energy window above 30 PE. This region corresponds to $(8.4 - 44.6)$ keV_{nr} (see Eq. 10).

In order to stay well above the trigger threshold which starts to roll off around 280 PE (see Fig. 2) a valid event is required to have $S2 > 300$ PE (uncorrected S2). The acceptance of such a condition affects the measured differential rate [see Eq. (18)] and is determined in the following way. For a given interval of position-corrected cS1 from $^{241}\text{AmBe}$ data, the position-corrected cS2 spec-

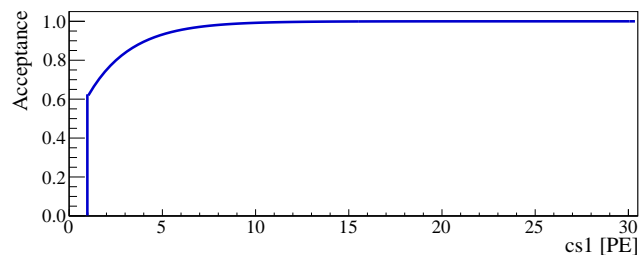


FIG. 7: Acceptance of the S2 threshold cut as a function of cs1, the S1 signal before Poisson fluctuations. The sharp drop at 1 PE was introduced artificially in order to be more conservative at the lowest signals. This acceptance is used in the WIMP rate calculation before the S1 signal is convoluted with a Poisson function to take statistical fluctuations into account.

trum is described in a functional form and extrapolated conservatively to the range below threshold. In order to minimize the extrapolation, only the top 7.5 cm of the detector are used for this analysis reducing the impact of charge losses due to the finite τ_e . From this data the acceptance $\epsilon_2(\text{cS1})$ of the $S2 > 300$ PE condition is determined numerically, taking into account the 48 kg fiducial mass, the increasing τ_e during science data taking, and the spatially uniform event distribution as expected from WIMP interactions.

This acceptance, however, cannot be simply applied to the observed science data as the measurement-related fluctuations of the S1 and S2 signals are independent from each other (see Sect. IIB). As an example, a recoil from a $7 \text{ GeV}/c^2$ WIMP can enter the detection region of $(8.4 - 44.6)$ keV_{nr} only because of upward fluctuations of the S1 scintillation signal. The average S2 signal of these events, however, is smaller than from WIMPs of higher masses, leading to a lower acceptance at the same S1 signal. The acceptance of the S2 threshold cut is therefore calculated as a function of the cs1 signal without Poisson fluctuations, which is proportional to the nuclear recoil energy deposition E_{nr} [see Eqs. (6)-(10)]. Since the nuclear recoil spectrum varies with the WIMP mass, this leads to a WIMP-mass-dependent acceptance (see Fig. 2 of [4]).

In general, cs1 and therefore the acceptance $\epsilon_{2,E}(\text{cs1})$ are experimentally not accessible. However, the latter can be determined indirectly from the previously derived $\epsilon_2(\text{cS1})$ from $^{241}\text{AmBe}$ data. Using $\mathcal{L}_{\text{eff}}(E_{\text{nr}})$ from [4] and Eq. (10), a $^{241}\text{AmBe}$ Monte Carlo simulated energy spectrum is converted into a cs1 signal spectrum. An initially estimated acceptance function $\epsilon_{2,E}^*(\text{cs1})$ is now applied to this spectrum and varied iteratively until the acceptance $\epsilon_2^*(\text{cS1})$ from the Monte Carlo dataset convoluted with a Poissonian distribution to account for the statistical fluctuations is equal to $\epsilon_2(\text{cS1})$. Figure 7 shows the resulting acceptance $\epsilon_{2,E}(\text{cs1})$. The acceptance is conservatively set to be 0 below 1 PE.

3. Selection of single scatter events

WIMPs are expected to scatter only once in the TPC producing one S1 and one S2 pulse in the waveform and no coincident signal in the veto volume. S2 pulses of a few PE size after the main S2 signal or small ionization signals from single electrons can bias the single scatter event selection as they can be mistaken as an S2 signal from a second scatter. It was observed that the size of these delayed signals is correlated with the size of the main S2 pulse. Thus, events with one S2 peak are selected by requiring all other S2 peaks to be smaller than a certain threshold value which was defined using nuclear recoil calibration data. However, the acceptance was calculated using electronic recoil science data, since the low-energy region was dominated by beta particle interactions which represent an almost pure single scatter event sample (see Sec. III F 2). The cut acceptance in the energy region of interest is $\gtrsim 95\%$ (see Fig. 4) and is independent of the S2 signal size.

Even in the case of an event with multiple scatters, only one S1 peak is expected since the 10 ns sampling time does not allow to distinguish between them. Multiple S1 signals in a waveform would come either from pile up (which is very unlikely given the low trigger rate of ~ 1 Hz during science data taking), PMT dark current, electronic noise, or misidentified uncorrelated S2 ionization signals from single electrons. Events where a second S1 peak is seen by at least two PMTs are therefore removed if it appears within the maximum possible drift time. However, if the S2/S1 ratio is too high for the second S1 candidate, the event is not rejected. Since this cut is affected by the noise conditions during the measurement, the acceptance was determined from the non-blinded science data to be $\sim 98.5\%$ in the $(4 - 30)$ PE energy range.

Given the negligible rate of accidental coincidences, a signal in the active LXe veto which is in coincidence with the S1 peak in the TPC must therefore be from a double scatter interaction. All events where a coincident signal in the veto is present with a size ≥ 0.35 PE are rejected. The non-blinded science data is used to calculate the acceptance of the cut, which is $> 99.6\%$.

4. Consistency cuts

Events were selected based on the comparison of the reconstructed position estimators from different algorithms, the fit quality of the reconstructed position, and the comparison of the measured S1 PMT pattern with the one expected from the reconstructed position. Interactions in the gaseous xenon or events with S1 and S2 signals not from the same physical interaction were also removed.

Large differences in the event positions inferred by the three different algorithms (see Sec. III C) in general correspond to unresolved multiple scatter events as their inter-

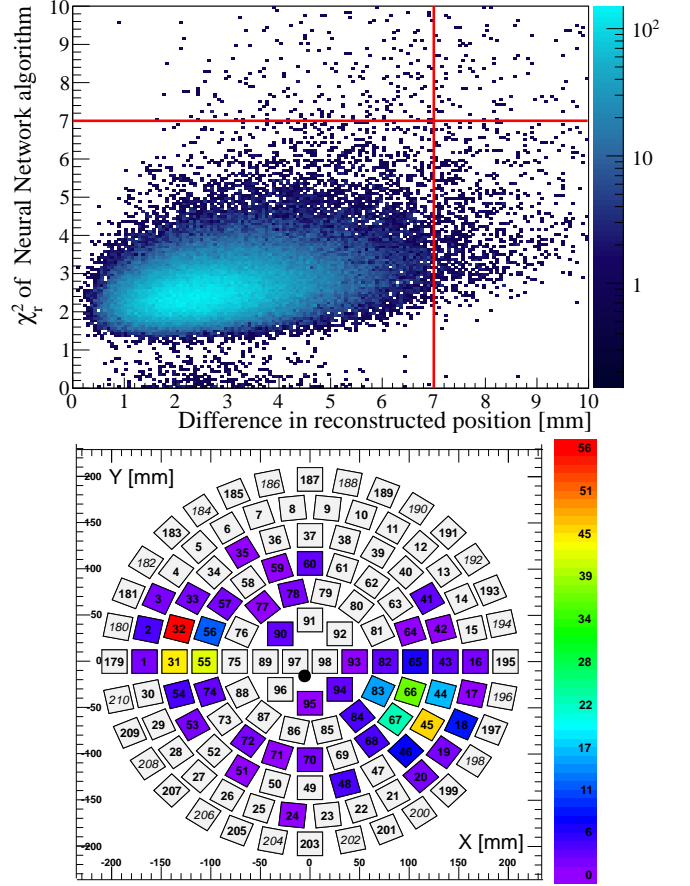


FIG. 8: Top: Neural network χ^2_r value versus the combined difference in the reconstructed position by the NN, SVM and χ^2 -minimization reconstruction algorithm from the $^{241}\text{AmBe}$ calibration data. Bottom: example of a double scatter event from neutron data rejected by the position reconstruction cuts. The PMT pattern of the top array clearly shows the presence of two S2 signals centered roughly on PMT 32 and 45, respectively. The black dot close to the center represents the reconstructed position. The color code of the legend represents the measured S2 signal size (in PE) seen by each PMTs.

actions are so close in z that the corresponding S2 signals cannot be separated. Events with the combined difference, calculated as the square-root of the sum of squared differences between (x, y) positions reconstructed by NN, SVM and χ^2 -minimization algorithms, larger than 7 mm are removed. A χ^2 -value of the difference between the observed S2 PMT hit pattern and the one expected from the Monte Carlo simulation quantifies the quality of the reconstruction position. Hence, a cut on the reduced χ^2_r value (χ^2 divided by the number of PMTs in the upper array) of the NN algorithm is used to reject badly reconstructed events. Figure 8 (top) shows the χ^2_r distribution of events calculated from an NN algorithm versus the combined difference in reconstructed position. Events above and on the right of the solid lines, are rejected. Figure 8 (bottom) shows the S2 PMT pattern of a dou-

ble scatter event which is rejected by these conditions. The position is reconstructed wrongly (black dot) close to PMT 97, in between the two true positions. The acceptance of these conditions is evaluated using ^{60}Co and $^{241}\text{AmBe}$ calibration data. It is $>99.6\%$ in the energy range of $(4 - 30)$ PE.

The width of an S2 pulse increases with the t_d due to the diffusion of the electron cloud during its propagation towards the gate grid. Typical width values, defined at 10% of its peak height, range from $\sim 1\mu\text{s}$ to $\sim 2\mu\text{s}$ for minimal and maximal ($t_d = 176\mu\text{s}$) drift times, respectively. The t_d -dependent S2 width is compared to the t_d value and events are rejected when these quantities are inconsistent. Neutron calibration data are used for the cut definition. Low energy S2 events show larger spread due to low statistics of drifted ionization electrons, hence the cut is defined in an energy-dependent way. The cut acceptance is set to 90% (see Fig. 4). The top panel of Fig. 9 shows the distribution of the S2 width versus t_d for nuclear recoil events from neutrons for all energies (blue). The red dots are the events removed by the S2 width selection. The waveforms in the middle and bottom panels correspond to accepted typical candidates with $t_d = 8\mu\text{s}$ and $t_d = 127\mu\text{s}$ between the S1 and S2 peak. Their uncorrected S2 sizes are ~ 1000 PE and ~ 1500 PE, respectively.

Multiple scatters from electromagnetic interactions in the science data or ^{60}Co calibration data, where one interaction happens inside the TPC and at least one in a charge insensitive region, can produce anomalous electronic-recoil leakage events. Such regions include the LXe volume below the cathode or close to the field shaping rings near the inner TPC wall. These events, referred to as “gamma-X”, are classified as valid single scatters because a single S2 is measured but the S1 is the sum of both prompt S1 signals. Having an S2/S1 ratio lower than that of true single scatters, the events can potentially leak into the WIMP search region.

The PMT hit pattern of the S1 signal is used to discriminate between these events and true single interactions. A likelihood parameter is computed as $-2\log(\lambda_P)$, where λ_P is the ratio of the Poisson likelihood of the measured S1 PMT pattern and the “standard” S1 PMT pattern of single scatter events which happen at the same reconstructed (x, y, z) position. The standard S1 PMT pattern map is acquired from the full absorption peak of ^{137}Cs calibration data. Figure 10 shows the distribution of the likelihood parameter for neutron data as a function of the uncorrected S1 signal area. Events with a poor likelihood ratio (above the line) are rejected because they have an S1 pattern that is inconsistent with the expectation based on their position. The acceptance of this cut is determined using ^{60}Co and $^{241}\text{AmBe}$ calibration data and is $\sim 97\%$ with no energy dependence.

Figure 11 shows an example of an event removed by the pattern likelihood selection which could be explained by a double scatter event with one interaction below the cathode. The top panel contains the pattern of the S2

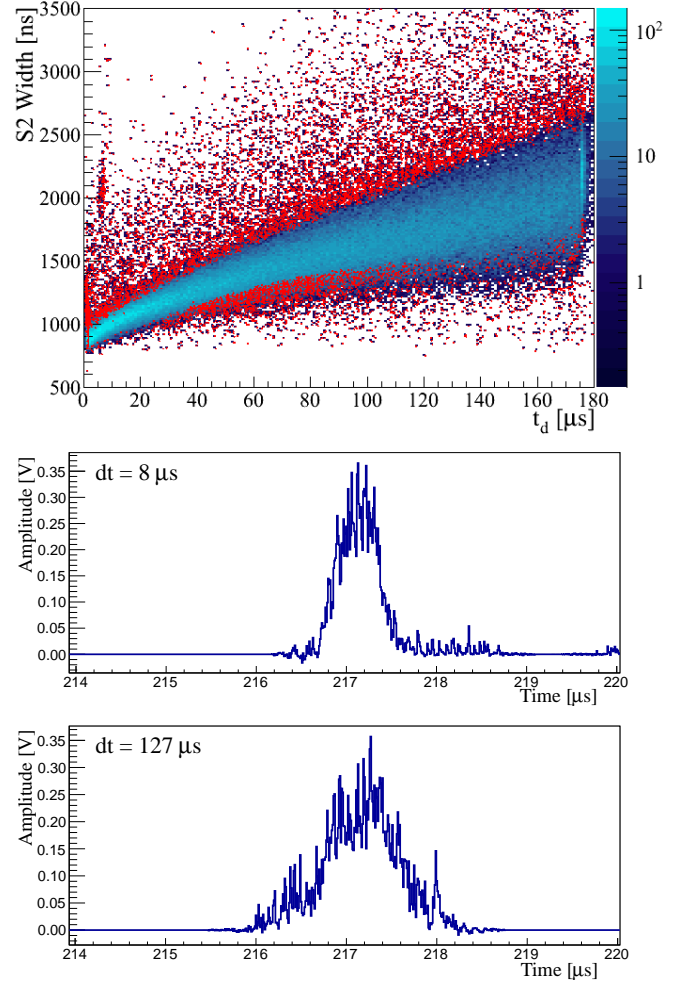


FIG. 9: Top: Distribution of the S2 width (defined at 10% of the peak height) versus drift time for nuclear recoils with energies up to 30 PE in S1 (blue histogram). The red dots are the events removed by the S2 width selection. Middle: S2 waveform example with $t_d = 8\mu\text{s}$. Bottom: S2 waveform example with $t_d = 127\mu\text{s}$.

signal in the top PMT array. The position is well reconstructed close to PMTs 72 and 87 (black dot). The bottom panel shows the pattern of the S1 signal in the bottom PMT array. The reconstructed z position is very close to the bottom PMT array, about 2.5 cm above the cathode grid and therefore the major part of the S1 light signal is seen around the (x, y) reconstructed position. In addition, there is a large portion of the S1 signal seen right above PMT 113 with no charge detected at similar (x, y) pointing to a possible second scatter below the cathode.

5. Signal/background discrimination and fiducial volume

Figure 12 shows the electronic and nuclear recoil bands from ^{60}Co (blue) and $^{241}\text{AmBe}$ (cyan) data, respectively,

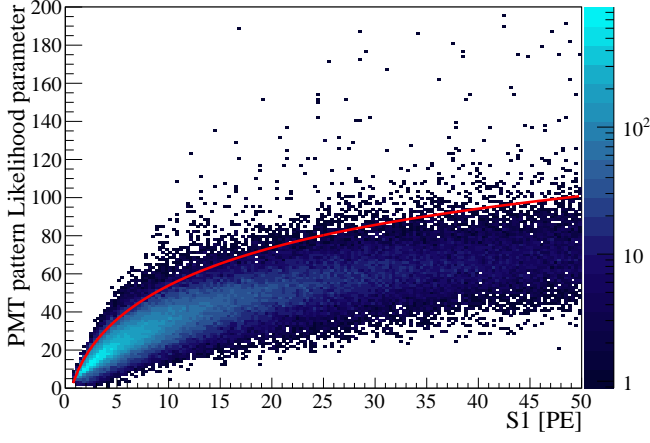


FIG. 10: Distribution of the likelihood parameter of the PMT pattern as a function of the uncorrected S1 signal for nuclear recoils. The likelihood parameter is computed as $-2 \log(\lambda_P)$, where λ_P is the ratio of the Poisson likelihood of the measured S1 PMT pattern and the “standard” S1 PMT pattern at the same position (see text). The red line represents the cut line above which events are discarded.

using the discrimination parameter $\log_{10}(S2_b/S1)$, flattened by subtracting the electronic recoil mean. This removes the energy dependence of the electronic recoil band allowing for an easier combination of data from different energies. The border lines of the 12 bands used by the Profile Likelihood analysis to model signal and background distributions are shown in red in the chosen energy window.

Compared to the Profile Likelihood analysis, the benchmark WIMP region for the cut-based analysis is additionally constrained by the S2/S1 electronic recoil rejection cut and the lower bound of the nuclear recoil band. The electronic recoil rejection level was defined using ^{60}Co calibration data which has an S2/S1 distribution is described well by a Gaussian function with an extra tail appearing about 3σ away from the mean value. It was set to 99.75% (see Fig. 12). The acceptance of this cut, calculated using nuclear recoils, is energy dependent and ranges from $\sim 29\%$ to $\sim 46\%$ (see Fig. 2 of [4]). The $^{241}\text{AmBe}$ data is used to constrain the signal region removing events which are more than 3σ away from the mean of the nuclear recoil band (see Fig. 12).

An ellipsoid containing 48 kg of liquid xenon is used as the fiducial target mass. Figure 13 shows the shape of the fiducial volume cut (red) together with the observed event distribution from the science data without applying any electronic recoil discrimination cut. The yellow dashed-contour represent the borders of the TPC. Events falling outside of it are due to the uncertainty in the position reconstruction. The background during this science run was dominated by ^{85}Kr which is uniformly distributed in the TPC as is visible in the central region of Fig. 13 (see also Sec. III F 2). For this reason, a smaller fiducial volume would not help to reduce the background

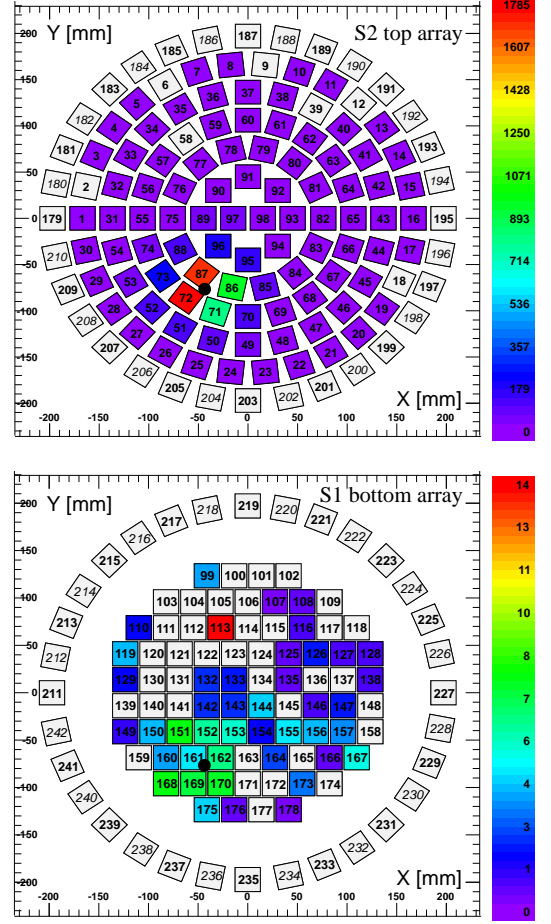


FIG. 11: Example of an event removed by the pattern likelihood selection. Top: The top array PMT pattern of the S2 signal with the reconstructed (x, y) position (black dot). Bottom: The bottom array PMT pattern of the S1 signal. This could be due to a double scatter event. One interaction happens below the cathode and close to the bottom PMT array resulting in a very localized S1 above PMT 113 with no corresponding S2 signal at similar (x, y) . The second interaction happens in the sensitive volume but still close to the cathode grid. Its (x, y) position is well reconstructed using the S2 signal in the top array, and its S1 signal is localized in several PMTs in the bottom array at similar (x, y) position, due to the vicinity of the interaction point.

further, and the largest possible volume was used instead. This choice was based mainly on the understanding of the spatial corrections in the detector. The edges of the detector are excluded as the position corrections are the largest in those regions. A few millimeters near the grids are removed to avoid the increased background in this region.

The $\log_{10}(S2_b/S1)$ distribution shows a population of events at low energies (few PE) and high values of the discrimination parameter, $\log_{10}(S2_b/S1) - \text{ER mean} > 0.5$. These correspond to random small S1 peaks that do not belong to the S2 signal. A dedicated cut removes these

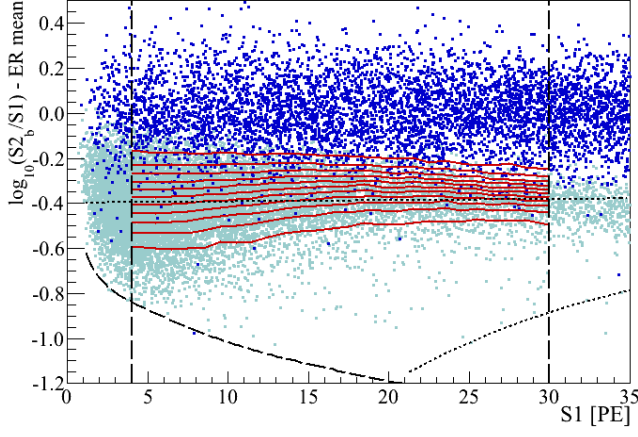


FIG. 12: Electronic (blue) and nuclear (cyan) recoil bands in flattened discrimination space. The black dashed lines, representing the analysis energy window (vertical) and the S2 threshold cut (bottom left), are used in both analysis methods. The 12 bands used in the Profile Likelihood analysis to model signal and background are shown in red. The benchmark WIMP region for the cut-based analysis is further constrained by the black dotted lines which are 99.75% electronic recoil rejection line (middle) and the lower 3σ contour of the neutron distribution (bottom right).

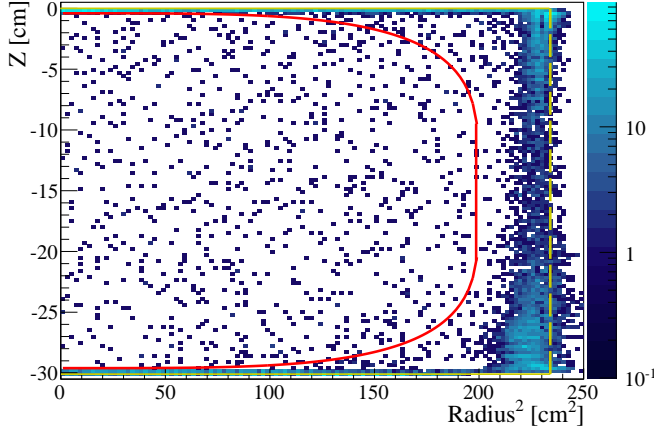


FIG. 13: Distribution of all events in the TPC observed in the $8.4 - 44.6 \text{ keV}_{\text{nr}}$ energy range during 100.9 live days. With the exception of the electronic recoil discrimination cut, all cuts are used including the ones introduced post-unblinding to remove a population due to electronic noise. The fiducial volume containing 48 kg of liquid xenon (red) and the TPC borders (yellow) are also indicated. Events outside of the borders are due to the uncertainty in the position reconstruction.

events which are far above the nuclear recoil band with an acceptance above 99.95%.

6. Overall cut acceptance

Figure 14 shows the overall acceptance of all cuts used for the Profile Likelihood analysis in the $(4 - 30) \text{ PE}$ S1 energy range and 48 kg fiducial mass. The solid line includes the published S1 coincidence requirement derived by a Monte Carlo simulation and the dotted line the improved acceptance using a data-driven method, see Fig. 4. The acceptance of the S2 threshold is shown in Fig. 7. The later has to be applied first to the WIMP spectrum without statistical fluctuations. Then the combination of all other cuts as shown in Fig. 14 is applied to the S1 spectrum after taking into account Poisson fluctuations. As already mentioned, for the cut-based analysis, the S2/S1 electronic recoil rejection cut and the 3σ lower nuclear contour are additionally applied (see Fig. 2 of [4]).

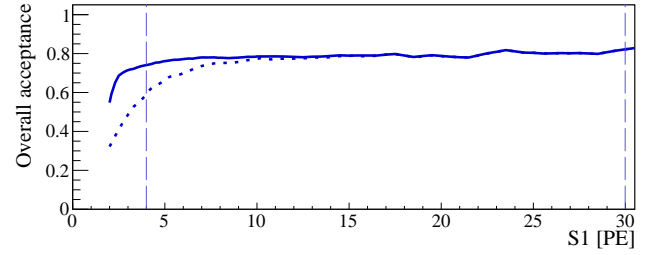


FIG. 14: Measured acceptance of all quality cuts as a function of the corrected S1 signal using the published S1 coincidence requirement derived by Monte Carlo (solid blue) and by a new data-driven method (dotted blue), see Fig. 4. The S2 threshold cut is treated separately (see Fig. 7). The two vertical dashed lines indicate the pre-defined energy window $(4 - 30) \text{ PE} = (8.4 - 44.6) \text{ keV}_{\text{nr}}$.

F. Background expectation

This section describes the various background contributions and quantifies the number of expected background events for the 100.9 live days exposure, the 48 kg fiducial mass and the benchmark region of the cut-based analysis defined in Sec. III D. The Profile Likelihood analysis uses exactly the same data and assumptions for the background estimation.

1. Nuclear recoil background from neutrons

The nuclear recoil background from muon-induced neutrons and from neutrons created in spontaneous fission and (α, n) reactions in the detector materials are determined using a GEANT4-based [25] Monte Carlo simulation [23]. Single scatter nuclear recoils in the LXe with no associated electronic recoil from inelastic reactions were selected assuming 3 mm event resolution.

Cosmogenic muons were simulated using the MUSIC [26] and MUSUN [27] packages. The muons and their

daughter particles from the electromagnetic and hadronic showers were propagated through the rock and through the XENON100 shield and detector materials. A total of $(0.08^{+0.08}_{-0.04})$ muon-induced events were found.

To obtain the neutron rate from natural radioactivity, the α -activity from the uranium and thorium chains is considered. These are derived from the detector material's γ -activities measured with germanium spectroscopy [9]. The neutron production rate in the detector and shield materials is computed using the α -activities from a modified SOURCES4A code [28, 29]. It calculates neutron production rates and energy spectra from (α, n) reactions and spontaneous fission. A total of (0.032 ± 0.006) neutron background events due to radioactive background were found.

Summing up all contributions, the total nuclear recoil background is $(0.11^{+0.08}_{-0.04})$ events, dominated by cosmogenic neutrons. The rather large errors are due to systematic uncertainties in the neutron production rates in the different materials [23].

2. Electronic recoil background from γ and β events

During the 100.9 live days run, the background at low energies was dominated by intrinsic ^{85}Kr (beta with 687 keV_{ee} endpoint), introduced accidentally through a tiny air leak in the gas system before the start of the dark matter search. The ^{85}Kr concentration was determined by comparing the measured energy spectrum to a detailed Monte Carlo simulation. The simulation includes the intrinsic radioactivity of all detector components, based on the measured contamination of the various materials. This method is described in detail in [14]. Assuming a ^{85}Kr isotopic abundance of 10^{-11} , a natural Kr concentration of (700 ± 100) ppt was obtained for the data presented here. In parallel, an analysis using delayed coincidences was performed to determine the ^{85}Kr concentration with an independent method [30]. It uses the decay of ^{85}Kr to ^{85m}Rb (beta with 173.4 keV_{ee} endpoint) followed by the decay of ^{85m}Rb to ^{85}Rb (gamma of 514 keV_{ee}) with 1.46 μs half-life and a branching ratio of 0.434%. Figure 15 shows the waveform of a ^{85}Kr candidate event. The natural Kr concentration, derived with

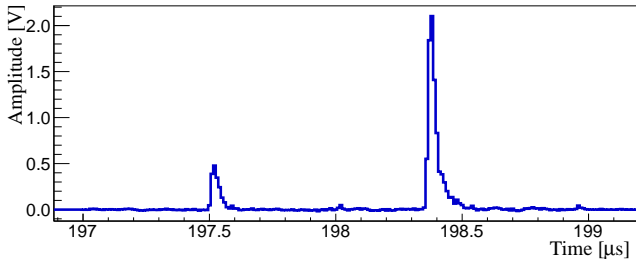


FIG. 15: S1 peaks of a candidate ^{85}Kr event where the second light signal from the γ -ray is delayed by ~ 900 ns.

this method, is compatible with the one inferred from the data/Monte Carlo comparison.

The electronic recoil background in the signal region consists of two contributions: leakage from the Gaussian shaped bulk of the electronic recoil background distribution and a small contribution of anomalous (non-Gaussian) leakage. The first is determined by extrapolating the low-energy science data of the non-blinded $\log_{10}(S2_b/S1)$ region. The prediction is (1.14 ± 0.48) events with the error being mainly due to the uncertainty in the definition of the electronic recoil discrimination level.

Events with incomplete charge collection contribute to the anomalous background. “Gamma-X” events as defined in Sec. III E 5 have such topology. β -decays from the dominating ^{85}Kr cannot create spatially-resolved multiple scatters due to the short electron mean free path, much less than the 3 mm position resolution. Therefore, ^{60}Co gamma calibration data was used to predict the anomalous background. The spatial distributions of anomalous events were found to be similar within 10% in the low energy region in Monte Carlo simulations of background and ^{60}Co calibration data. This was also confirmed by comparing spatial and energy distributions of potential leakage candidates, selected using the S1 pattern likelihood parameter, in the ^{60}Co calibration data and low-energy non-blinded science data. Taking into account the different exposure of the ^{60}Co calibration compared to the science data, and the fraction of the background due to gamma interactions that can undergo multiple scatters, the anomalous leakage into the signal region was estimated to be $(0.56^{+0.21}_{-0.27})$ events. The error includes the anomalous leakage discrepancy in the calibration and background distributions and the uncertainty in the estimation of the ^{85}Kr concentration in the LXe.

3. Total background expectation and side-band test

TABLE I: Contributions to the total background prediction for the benchmark WIMP search region, 100.9 live days exposure and 48 kg fiducial mass.

Source	Expected background
ER Gaussian leakage	(1.14 ± 0.48) events
ER anomalous leakage	$(0.56^{+0.21}_{-0.27})$ events
NR from neutrons	$(0.11^{+0.08}_{-0.04})$ events
Total	(1.8 ± 0.6) events

Taking into account all background sources mentioned above, the total background prediction for the benchmark WIMP search region, 100.9 live days exposure and 48 kg fiducial mass is (1.8 ± 0.6) events. Table I summarizes the background contributions. Alpha decays in the LXe do not contribute to the background as they have

energies of a few MeV, far above the energy region of interest for the dark matter search.

Before analyzing the science data in the region of interest, the side-band region (30 – 130) PE was unblinded. The background predictions for the 99.5%, 99.75% and 99.9% discrimination levels were $14.3^{+7.7}_{-8.5}$, $8.2^{+2.2}_{-2.6}$ and $5.6^{+0.6}_{-1.0}$ events while 10, 8 and 7 events were observed, respectively. The observed and predicted numbers of events are compatible within the errors confirming the validity of the background predictions.

G. Observed event population

Figure 16 shows the final distribution of events in the electronic/nuclear recoil discrimination parameter (see Sec. III E 5) as a function of nuclear recoil energy E_{nr} . Based on the comparison of the observed event distribution with the background-like distribution from Monte Carlo simulations, the background-only hypothesis was tested using a Profile Likelihood method [22]. The p -value for this hypothesis, which is the probability that the outcome of a hypothetical XENON100 experiment results in an observation equal or less background-like than the observed one, was found to be 31%.

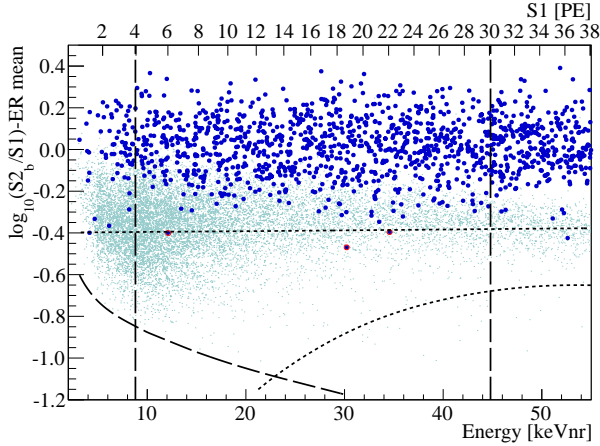


FIG. 16: The electronic/nuclear recoil discrimination parameter as a function of nuclear recoil energy. Blue points indicate the observed event distribution after all cuts. Cyan points show the nuclear recoil distribution as measured with an $^{241}\text{AmBe}$ neutron source. The dashed-lines represent the energy window 8.4 – 44.6 keV_{nr} and the threshold cut $S2 > 300$ PE. The dotted-lines indicate the 99.75% rejection line from above and the 3σ contour of the NR distribution from below. These are not used in the Profile Likelihood analysis, but are used to define the benchmark WIMP region. Three events with energies of 12.1, 30.2 and 34.6 keV_{nr} fall into the benchmark region (red circles). This plot shows the same event distribution as Fig. 3 in [4].

In the pre-defined benchmark WIMP search region, three events remain after all cuts. These events with energies of 12.1, 30.2 and 34.6 keV_{nr}, as derived from their

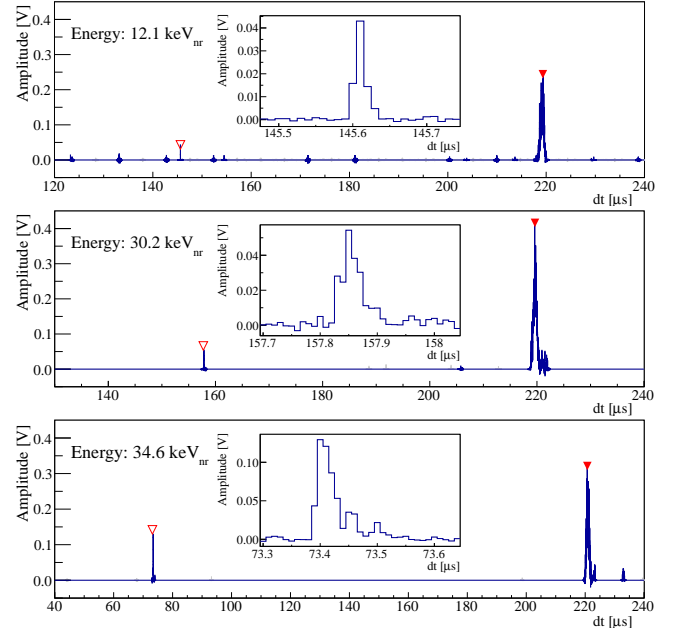


FIG. 17: Waveforms of the three events in the benchmark region that pass all cuts, including the ones defined post-unblinding. The S1 peaks are labelled by open triangles, while the S2 peaks are labelled by full triangles. The insets show an expanded view around the S1 region. Periodic electronic noise is visible in the top event, while single electron pulses after the major S2 at the trigger position (220 μs) are visible in the bottom event.

S1 signal, are marked by red circles in Fig. 16. The events are homogeneously distributed inside the fiducial volume, as can be seen in Fig. 4 of reference [4]. Their waveforms are shown in Fig. 17. Though one of the events shows presence of periodic electronic noise in the waveform (top panel), the S1 signal has a higher amplitude and is not affected by it. The other two events have no noise present in their waveform (middle and bottom panels).

Within the background expectation of (1.8 ± 0.6) events, the 3 observed events do not constitute an evidence for dark matter as the probability of a Poisson process with an expectation value of 1.8 events to fluctuate up to 3 or more events is 28%. This is consistent with the p -value of the Profile Likelihood model. Therefore, exclusion limits on spin-independent elastic and inelastic WIMP-nucleon scattering interaction were placed in [4] and [5].

IV. SUMMARY AND OUTLOOK

A detailed description of the analysis of the 100.9 live days of science data acquired by XENON100 in 2010 is presented. The data set, the selection criteria, the evaluation of the cut acceptances and the background estimates have been described. This data had been used to derive results in terms of spin-independent elastic

[4] and inelastic [5] WIMP-nucleon interactions. However, the methods presented here are general in nature and also apply to forthcoming XENON100 dark matter search data. Several improvements have been made on data quality cuts against electronic noise and position-dependent corrections of the measured signals using the significantly larger amount of both electronic and nuclear recoil calibration data. The most stringent limits to date on both spin-independent elastic and inelastic WIMP-nucleon cross sections demonstrated already the potential of the XENON100 detector. A further refinement of the analysis, an improved detector performance and a greater exposure will increase the level of sensitivity of the XENON100 experiment.

V. ACKNOWLEDGEMENTS

We gratefully acknowledge support from NSF, DOE, SNF, Volkswagen Foundation, FCT, Région des Pays de la Loire, STCSM, NSFC, DFG, Stichting voor Fundamenteel Onderzoek der Materie (FOM), and the Weizmann Institute of Science. T.M.U. acknowledges the Alexander von Humboldt Foundation for support through a Feodor Lynen scholarship. We are grateful to LNGS for hosting and supporting XENON100.

-
- [1] N. Jarosik et al., *Astrophys. J. Suppl.* **192**, 14 (2011), [arXiv:1001.4744](#).
 - [2] G. Jungman, M. Kamionkowski, and K. Griest, *Phys. Rept.* **267**, 195 (1996), [arXiv:hep-ph/9506380](#).
 - [3] M. W. Goodman and E. Witten, *Phys. Rev. D* **31**, 3059 (1985).
 - [4] E. Aprile et al. (XENON100), *Phys. Rev. Lett.* **107**, 131302 (2011), [arXiv:1104.2549](#).
 - [5] E. Aprile et al. (XENON100), *Phys. Rev.* **D84**, 061101 (2011), [arXiv:1104.3121](#).
 - [6] E. Aprile et al. (XENON100), *Astropart. Phys.* **35**, 573 (2012), [arXiv:1107.2155](#).
 - [7] E. E. Schwentner, N. Koch and J. Jortner, *Electronic Excitations in Condensed Rare Gases.*, vol. 107 (Springer Tracts in Modern Physics, Springer-Verlag, 1985).
 - [8] A. Lansiart et al., *Nucl. Instr. and Meth.* **135**, 47 (1976), ISSN 0029-554X.
 - [9] E. Aprile et al. (XENON100), *Astropart. Phys.* **35**, 43 (2011), [arXiv:1103.5831](#).
 - [10] M. Aglietta et al. (LVD), *Phys. Rev. D* **58**, 092005 (1998).
 - [11] E. Dahl, Ph.D. thesis, Princeton University (U.S.A) (2009).
 - [12] G. Plante et al., *Phys. Rev.* **C84**, 045805 (2011), [arXiv:1104.2587](#).
 - [13] F. Bezrukov, F. Kahlhoefer, and M. Lindner, *Astropart. Phys.* **35**, 119 (2011), [arXiv:1011.3990](#).
 - [14] E. Aprile et al. (XENON100), *Phys. Rev.* **D83**, 082001 (2011), [arXiv:1101.3866](#).
 - [15] E. Santos et al., *JHEP* **12**, 115 (2011).
 - [16] E. Aprile et al., *Phys. Rev. Lett.* **97**, 081302 (2006), [arXiv:astro-ph/0601552](#).
 - [17] I. Antcheva et al. (ROOT), *Comput. Phys. Commun.* **180**, 2499 (2009).
 - [18] A. Hitachi et al., *Phys. Rev. B* **27**, 5279 (1983).
 - [19] G. Plante, Ph.D. thesis, Columbia University (USA) (2012), URL http://xenon.astro.columbia.edu/XENON100_Experiment/Publications/.
 - [20] A. Zell et al. (Stuttgart Neural Network Simulator), URL <http://www.ra.cs.uni-tuebingen.de/SNNS/>.
 - [21] C. Chang and C. Lin (LIBSVM a library for support vector machines), URL <http://www.csie.ntu.edu.tw/~cjlin/libsvm/>.
 - [22] E. Aprile et al. (XENON100), *Phys. Rev.* **D84**, 052003 (2011), [arXiv:1103.0303](#).
 - [23] A. Kish, Ph.D. thesis, University of Zurich (Switzerland) (2011), URL <http://opac.nebis.ch/ediss/20121322.pdf>.
 - [24] S. Yellin, *Phys. Rev.* **D66**, 032005 (2002), [arXiv:physics/0203002](#).
 - [25] J. Sulkimo (GEANT4), *Nucl. Instrum. Methods Phys. Res. Sect. A* **506**, 250 (2003).
 - [26] P. Antonioli et al., *Astropart. Phys.* **357** (1997).
 - [27] V. A. Kudryavtsev, *Comp. Phys. Comm.* **180**, 339 (2009), [arXiv:0810.4635](#).
 - [28] W. Wilson, SOURCES4A, Technical Report LA-13539-MS, Los Alamos (1999).
 - [29] M. J. Carson et al., *Astropart. Phys.* **21**, 667 (2004), [arXiv:hep-ex/0404042](#).
 - [30] G. Alimonti et al. (Borexino Collaboration), *Astroparticle Physics* **16**, 205 (2002), [arXiv:hep-ex/0012030](#).